RESEARCH ARTICLE

NANO · MICRO small
www.small-journal.com

Transforming *Spirulina maxima* Biomass into Ultrathin Bioactive Coatings Using an Atmospheric Plasma Jet: A New Approach to Healing of Infected Wounds

Tuyet Pham, Tien Thanh Nguyen, Ngoc Huu Nguyen, Andrew Hayles, Wenshao Li, Duy Quang Pham, Chung Kim Nguyen, Trung Nguyen, Jitraporn Vongsvivut, Neethu Ninan, Ylias Sabri, Wei Zhang, Krasimir Vasilev, and Vi Khanh Truong**

The challenge of wound healing, particularly in patients with comorbidities such as diabetes, is intensified by wound infection and the accelerating problem of bacterial resistance to current remedies such as antibiotics and silver. One promising approach harnesses the bioactive and antibacterial compound C-phycocyanin from the microalga *Spirulina maxima*. However, the current processes of extracting this compound and developing coatings are unsustainable and difficult to achieve. To circumvent these obstacles, a novel, sustainable argon atmospheric plasma jet (Ar-APJ) technology that transforms *S. maxima* biomass into bioactive coatings is presented. This Ar-APJ can selectively disrupt the cell walls of *S. maxima*, converting them into bioactive ultrathin coatings, which are found to be durable under aqueous conditions. The findings demonstrate that Ar-APJ-transformed bioactive coatings show better antibacterial activity against *Staphylococcus aureus* and *Pseudomonas aeruginosa*. Moreover, these coatings exhibit compatibility with macrophages, induce an anti-inflammatory response by reducing interleukin 6 production, and promote cell migration in keratinocytes. This study offers an innovative, single-step, sustainable technology for transforming microalgae into bioactive coatings. The approach reported here has immense potential for the generation of bioactive coatings for combating wound infections and may offer a significant advance in wound care research and application.

1. Introduction

Wound infection and subsequent healing impairment is a complex process with a significant global impact, affecting millions of individuals worldwide.[1,2] In particular, chronic wounds result in substantial morbidity due to extended healing times and often the inability to heal.[3] This ubiquitous problem highlights the need for innovative materials and methods capable of enhancing wound healing and the rate of recovery. Beyond alleviating symptoms, such as pain, effective wound treatment can help reduce hygiene-related complications and the risk of infection, which pose serious threats to successful healing. The clinical need, combined with the growing wound care product market, projected to reach between $15 and $22 billion annually by 2024,[4] underscores the opportunities for the introduction of novel wound treatments.

Wound infections arise from contamination by pathogenic bacteria, leading to tissue colonization and the expression of

T. Pham, T. T. Nguyen, N. H. Nguyen, A. Hayles, W. Li, D. Q. Pham, C. K. Nguyen, N. Ninan, K. Vasilev, V. K. Truong
Biomedical Nanoengineering Laboratory
College of Medicine and Public Health
Flinders University
Adelaide, SA 5042, Australia
E-mail: krasimir.vasilev@flinders.edu.au; vikhanh.truong@flinders.edu.au

T. T. Nguyen
College of Medicine and Pharmacy
Tra Vinh University
Tra Vinh 87000, Vietnam

N. H. Nguyen
School of Biomedical Engineering
University of Sydney
Darlington, NSW 2006, Australia

D. Q. Pham
School of Engineering
Swinburne University of Technology
Hawthorn, VIC 3122, Australia

C. K. Nguyen, Y. Sabri
School of Engineering
RMIT University
Melbourne, VIC 3000, Australia

The ORCID identification number(s) for the author(s) of this article can be found under https://doi.org/10.1002/smll.202305469

DOI: 10.1002/smll.202305469

virulence factors.[1,2,5] Factors influencing wound infections highly depend on the type of wound, the patient's overall health status, and the healthcare environment. With an estimated 1%–3% of all surgeries in the United States resulting in surgical site wound infections, and up to 50% of diabetic foot ulcers becoming infected,[1] the management of wound infections is of paramount importance. Antibiotic treatment is the principal intervention used to curtail infections.[1,2] The overuse and misuse of antibiotics are known to lead to the development of antibiotic resistance and are rapidly becoming the most urgent problem in healthcare.[6] Silver-based dressings have been widely used in the treatment of infected wounds.[7–9] Nevertheless, the wound-healing effectiveness of these dressings is compromised by the cumulative toxicity of silver.[10,11] Furthermore, a concerning development is the emergence of bacterial silver resistance in wound care, posing a serious challenge.[8,12,13]

Microalgae, such as *Spirulina maxima*, have emerged as a promising alternative in the quest for effectively treating wound infections.[14,15] It is worth to note here that *S. maxima* has the most recent scientific name *Limnospira maxima*;[16] however, due to the common use, *S. maxima* name is used throughout this study. These unicellular organisms possess a simple reproductive system that generates a biomass containing bioactive compounds, including phycocyanin, anthocyanin, and active oligosaccharides.[16–18] Notably, these microalgae exhibit potent antioxidant activity that can counter the damaging effects of inflammation at the site of the wound, as well as strong antibacterial properties crucial for preventing infections.[14,15] Nevertheless, harnessing the full potential of these microalgae for wound care has traditionally been limited by several key challenges.[19,20] An important challenge arises when attempting to extract, refine, and encapsulate the valuable compounds derived from microalgae. The thick cell walls of microalgae, which serve as a protective barrier in their natural aquatic habitats, pose a significant obstacle, rendering the extraction processes inefficient.[19,20] Further complexity to the refinement and encapsulation procedures can lead to the degradation or loss of the bioactive compounds, consequently diminishing their potential benefits for wound healing.

In this study, we present an innovative approach to develop ultrathin coatings derived from *S. maxima*, integrating biotechnology and plasma physics. With the increasing demand and interest in antibacterial coatings, plasma techniques have gained significant prominence.[21–23] Herein, we harness the capability of an atmospheric plasma jet operated in an inert argon gas, to convert single cells of *S. maxima* biomass into a durable and functional bioactive ultrathin coating (refer to **Scheme 1**). Using this technology, we succeed not only to ensure the preservation of all bioactive compounds within the biomass but also to enable the breakdown of polysaccharides present in the microalgal cell wall. The resulting formation of bioactive linkages significantly enhances the bioavailability of the wound-healing compounds present in the microalgal cells. The bioactive coatings produced from this process exhibit an ensemble of healing properties including promotion of skin cell proliferation and expediting wound closure. Moreover, the coatings possess anti-inflammatory properties, which are crucial in the management of wound-related inflammation and pain, and ensuring effective wound healing.[24,25] Importantly, the coatings display potent antibacterial characteristics, offering a protection from wound infections and reducing the need for antibiotics, and the associated problems with the development of resistance. To the best of our knowledge, our pioneering technology is the first of its kind capable of transforming single microalgal cells into a functional bioactive coating. Our approach could offer a comprehensive solution for wound healing via harnessing the full therapeutic potential of *S. maxima* using a plasma-assisted transformation of algal biomass into efficient and cost-effective coatings.

2. Results and Discussion

2.1. Designing and Characterizing Argon Atmospheric Plasma Jet Process to Transform *S. maxima* Biomass into an Ultrathin Coating

The robust cell wall of *S. maxima* presents a considerable barrier to the utilization of its bioactive compounds.[19,20] In response to this challenge, we have developed a novel argon atmospheric plasma jet (Ar-APJ) system, capable of selectively disrupting the polysaccharide structures within the algal cell wall. The inertness of argon plasma jet is ideal for transforming the sensitive biological material of *S. maxima*. This technique not only allows for the reforming the polysaccharide fragments within the cell wall, but also preserves the essential bioactive compounds. The successful manipulation of polysaccharide linkages paves the way for producing contiguous coatings directly from microalgae biomass. A detailed schematic of the argon plasma jet system can be found in **Figure 1**A,B and Text S1 (Supporting Information). Optical emission spectroscopy was utilized to provide the comprehensive characterizations for our Ar-APJ system, as detailed in Text S2 and Figure S1 (Supporting Information). A typical optical emission spectrum and the corresponding emission bands covering a range of 200–950 nm are shown in Figure 1C. The peaks in the wavelength range of 690–912 nm are attributed to the 4p→4s transition of the excited argon species.[26] The peaks observed at 316, 337, 357, 380, and 405 nm are associated with the second positive system (SPS) of molecular nitrogen N_2 ($C^3\Pi_u \rightarrow B^3\Pi_g$, $\Delta v = 0$).[27] The generation of the N_2 ($C^3\Pi_u$) emission is attributed to the excitation of ground-state N_2 ($X^1\Sigma_g^+$) molecules by electron collisions, as shown in Equation (1). On the other

T. Nguyen
College of Science and Engineering
Flinders University
Adelaide, SA 5042, Australia
J. Vongsvivut
Infrared Microspectroscopy Beamline
ANSTO Australian Synchrotron
Clayton, Victoria 3168, Australia
Y. Sabri
Centre for Advanced Materials & Industrial Chemistry (CAMIC)
School of Science
RMIT University
GPO Box 2476, Melbourne, VIC 3001, Australia
W. Zhang
Advanced Marine Biomanufacturing Laboratory
Centre for Marine Bioproduct Development
College of Medicine and Public Health
Flinders University
Adelaide 5042, Australia

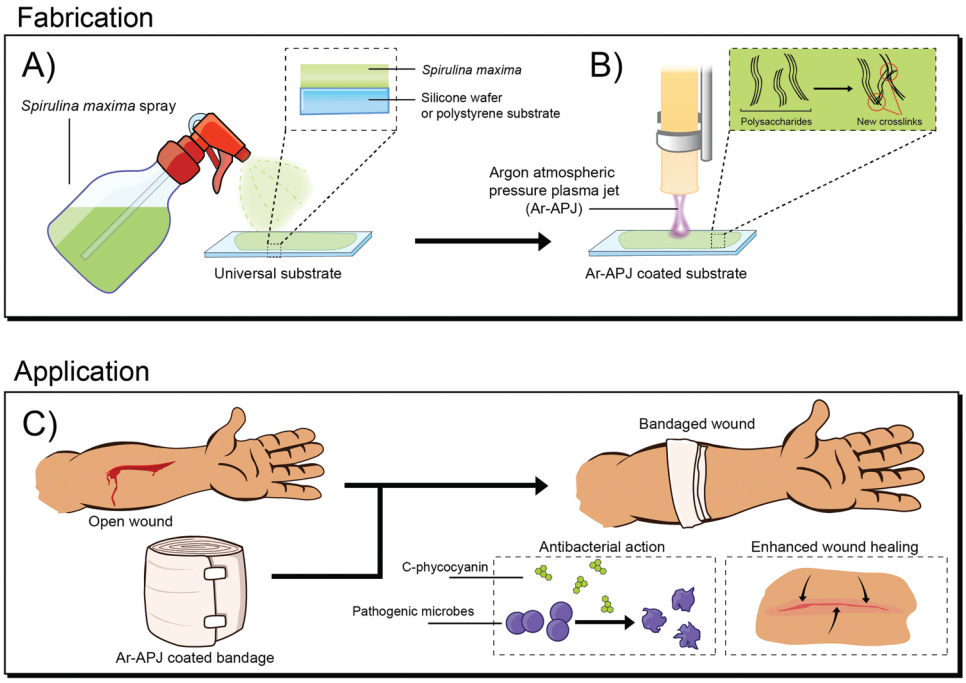

Scheme 1. A schematic depicting the one-step argon atmospheric pressure plasma jet (Ar-APJ) process to transform *S. maxima* biomass into an ultrathin bioactive coating. A) *S. maxima* is sprayed onto a universal substrate. B) Ar-APJ process transforms the *S. maxima* biomass into a durable, bioactive, ultrathin coating. C) Antibacterial wound dressings as a proposed application for the Ar-APJ technology.

hand, the low-lying N_2 ($B^3\Sigma_g^+$) emission is associated with the de-excitation transitions of N_2 ($C^3\Pi_u$), as described by Equation (2).[28]

$$e^- + N_2\left(X^1\sum_g^+\right)v = 0 \rightarrow N_2(C^3\Pi_u)v' = 0 + e^- \quad (1)$$

$$N_2(C^3\Pi_u) \rightarrow N_2\left(B^3\sum_g^+\right) + h\nu \quad (2)$$

The detection of an emission peak of ·OH at 309 nm corresponding to $A^2\Sigma^+ \rightarrow X^2\Pi$ ($\Delta v = 0$) indicates the dissociation of water molecules by high-energy electron collisions [Equation (3)] and the Penning process with excited argon and water vapor [Equation (4)].[28]

$$e^- + H_2O \rightarrow e^- + H + \cdot OH \quad (3)$$

$$Ar^* + H_2O \rightarrow Ar + H + \cdot OH \quad (4)$$

The atomic oxygen lines observed at 777 and 844 nm are the result of the $2s^22p^3(^4S^0)3s \rightarrow 2s^22p^3(^4S^0)3p$ transition induced by electron impact collisions with oxygen molecules, as given in Equation (5).[28] The generated O can potentially recombine with H radicals, ultimately leading to the formation of ·OH, as described in Equation (6).[29]

$$O_2 + e^- \rightarrow 2O + e^- \quad (5)$$

$$O + H + M \rightarrow \cdot OH + M \quad (6)$$

It should be noted that despite the use of argon carrier gas, the OES shows the presence of nitrogen and oxygen species that are unavoidable in processes carried out in ambient air.[29] The OES spectrum also shows peaks corresponding to the generation of reactive oxygen and nitrogen species (RONS) during treatment, which can further break down *S. maxima* cell walls, turning them into a robust coating with further treatments (Figure 1D). Three different voltages (5.2, 7.6, and 10 kV) and three gas flow rates (5, 10, and 20 liters per minute [LPM]) were selected to generate argon plasma. The results of optical emission spectroscopy[11] reflecting the Ar-APJ conditions are presented in Figure S2 (Supporting Information). The optimal condition for generating the maximum plasma intensity, namely, 10 LPM at 10 kV, was selected for the treatment of *S. maxima*. A summary of the selected conditions is shown in Table S1 (Supporting Information).

Furthermore, the Ar-APJ treatment designed in this study is a substrate-independent process, meaning that the coatings can be prepared on almost any type of biomaterial. The preparation of plasma-treated *S. maxima* coatings directly on commercial wound dressing is shown in Figure S13 (Supporting Information).

2.2. Effects of Ar-APJ on *S. maxima* Biomass

Before the Ar-APJ treatment, the surfaces of silicon wafers or coverslips were precoated with *S. maxima* with a density of 0.1 mg cm^{-2}. The cell viability of *S. maxima* biomass was found to be completely dead, shown in Text S3 (Supporting Information). The cell wall of *S. maxima* can be stained with a 0.01% (w/v) calcofluor white solution, so cell walls can be visualized under

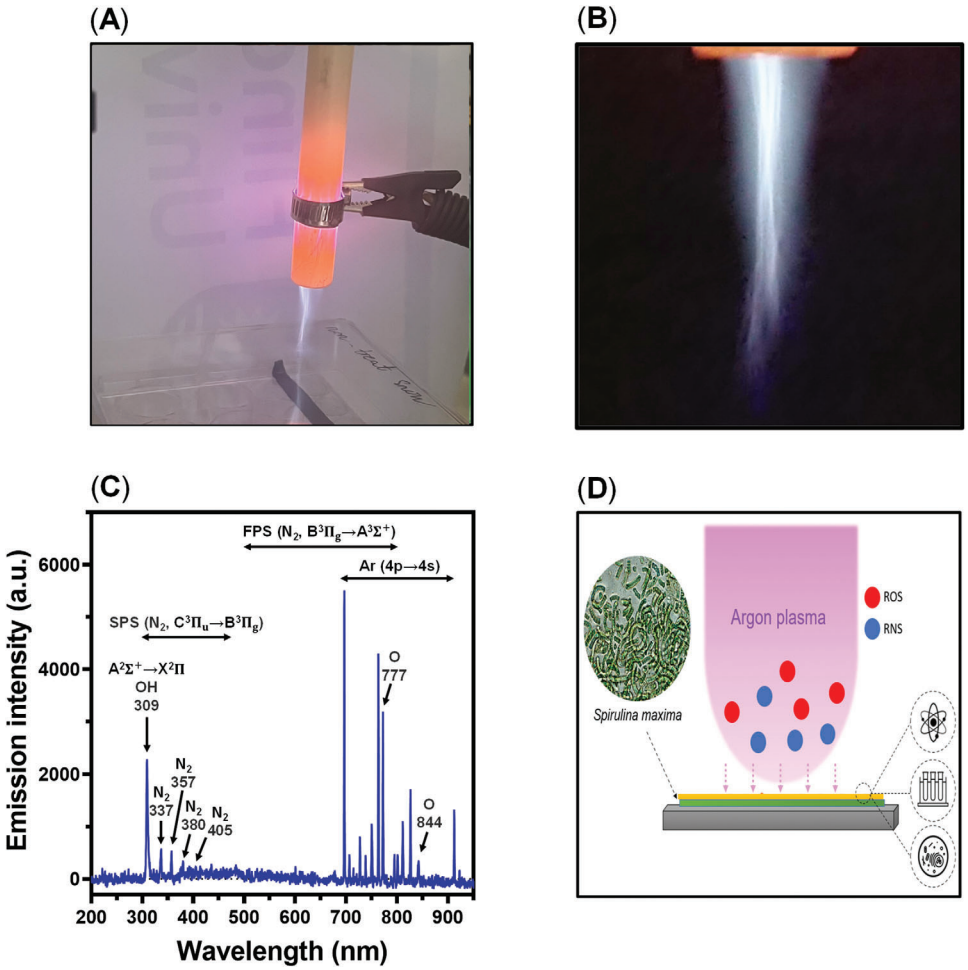

Figure 1. Overview of argon atmospheric plasma jet (Ar-APJ) system. A) Photograph showing the setup argon atmospheric plasma treatment (Ar-APJ) used to transform *S. maxima* biomass into a robust ultrathin coating. B) Photograph showing the argon atmospheric plasma jet (Ar-APJ). C) OES spectra of Ar-APJ at the argon flow rate of 10 LPM and voltage at 10 kV. D) Illustration of how Ar-APJ can turn *S. maxima* into a contiguous ultrathin coating.

the epifluorescence microscope (**Figure 2**). Scanning electron microscopy (SEM) was employed to examine the microalgae morphology post Ar-APJ treatments. The initial condition of untreated *S. maxima* revealed an intact cell wall and morphology, with a length of ≈40 ± 10 µm (Figure 2A). Upon subjecting a 100-s Ar-APJ treatment to a 1 cm^2 area, the cell wall underwent fragmentation into smaller segments, each ≈20–25 µm in length (Figure 2B). Although the majority of the cell wall remained intact, the treatment caused noticeable cracks on the microalgal surfaces. Further extending the treatment time to 200 s across 1 cm^2 area resulted in a significant transformation. *S. maxima* lost its native structure, completely disintegrated, and subsequently reformed into ultrathin films (Figure 2C). For a more comprehensive analysis of the effects of Ar-APJ on *S. maxima*, see detailed discussions in Text S4 (Supporting Information), along with Figures S4 and S5 (Supporting Information).

These observations align with previous studies demonstrating the capacity of atmospheric plasma treatment to disrupt only the peptidoglycan layer of bacteria.[30,31] The degree of cell disruption depends on the treatment duration.[32] The high-energy and reactive species generated during the plasma treatment procedure induce chemical reactions within the cell wall, causing the breakage of intermolecular bonds and the rearrangement of molecular structures.[33,34] Moreover, reactive species generated from the plasma treatment, such as reactive oxygen species (ROS) and reactive nitrogen species,[35] have been shown to interact with and modify the cell wall components of microalgae, affecting the physicochemical properties of the cell wall, including surface charge, hydrophobicity, and permeability.[36]

Based on these observations, the Ar-APJ treatments of 200 s over 1 cm^2 are selected for further studies. Henceforth, untreated *S. maxima* coatings will be annotated as Sm, and plasma-treated coatings will be annotated as PSm. Notably, we found that APJ-treated coatings (PSm) exhibit resilience and durability against multiple washings with water. These plasma-treated coatings remain intact even after being submerged in water for a duration of 24 h and even under the flow of water (Text S12, Figure S12, and Video S1, Supporting Information). The durability of PSm demonstrates that the thin coating will remain intact and will not delaminate when it is applied to its intended wound site. This property enables the coating to remain in place and provide a sustained release of bioactive compounds, such as phycocyanin. The

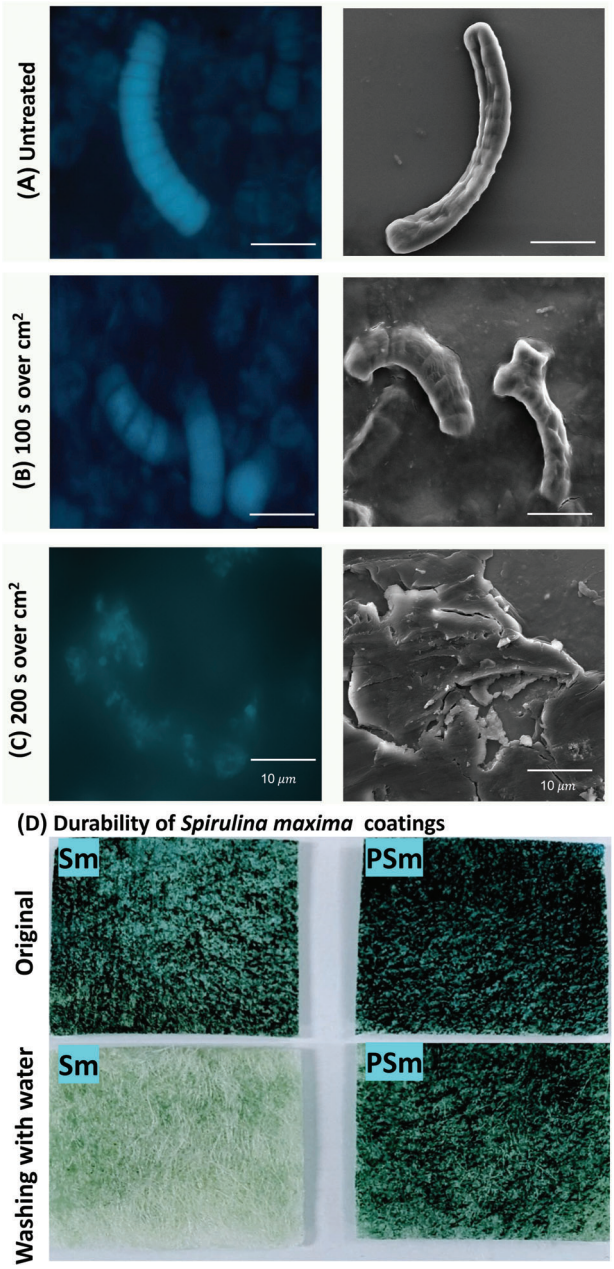

Figure 2. Morphological analysis of *S. maxima* following Ar-APJ treatment, observed using epifluorescence (left) and scanning electron microscopy (SEM) (right) imaging techniques. Morphology of A) untreated *S. maxima*. *S. maxima* treated with Ar-APJ for a duration of B) 100 s and C) 200 s over a surface area of 1 cm^2, resulting in significant changes in the cell wall structure. D) Photographs showing the durability of coatings of untreated (Sm) and treated *S. maxima* (PSm) with the conditions of 200 s m^{-2}. Original coatings of Sm and PSm were then washed with water to examine their durability.

sustained release of these bioactive compounds can inhibit bacterial growth and support the wound healing process. The data are shown in Figure S10 and Text S8 (Supporting Information).

The water contact angle results indicate that all PSm samples exhibit greater wettability compared to the corresponding Sm samples at the respective concentrations (Figure S11, Supporting Information). At an algae concentration of 0.1 mg cm^{-2} on the surface, the water contact angle of PSm and Sm was 27.7° ± 4.6 and 43.1° ± 3.1, respectively. This trend was also observed at a coating concentration of 0.6 mg cm^{-2}, where the corresponding contact angle of PSm and Sm was 23.5° ± 2.9 and 59.6° ± 2.8, respectively. Consequently, the surface treatment using Ar-APJ appears, involving algae coating at both concentration ranges, significantly enhanced the wettability of the PSm samples.

2.3. Analysis of Changes of Functional Groups of *S. maxima*

To characterize the biomolecular changes to the structural components of *S. maxima* following Ar-APJ treatment, we used synchrotron-sourced macro attenuated total reflection Fourier-transform infrared (ATR-FTIR) microspectroscopy.[37,38] **Figure 3**A shows representative spectral maps of the regions of interest as a function of FTIR absorption intensity. This was generated by integrating the spectral region for lipids in the methylene region (3000–2800 cm^{-1}), for proteins in the amide region (1705–1600 cm^{-1}), and for polysaccharides and nucleic acid changes in the fingerprint region (1200–950 cm^{-1}). The heat maps indicate variations in the intensity of these regions. Although the maps are normalized, a decrease in intensity in the C—H and fingerprint spectral regions can be observed after plasma treatment, along with an increased intensity of amide I and II peaks. These observations may indicate cellular breakdown, leading to the leakage of intracellular components. We conducted principal component analysis (PCA) to identify distinct changes in the ATR-FTIR spectra between treated and untreated substrates, as shown in Figure 3B. With PC-1 describing 90% of the spectral variation between samples, the two sets were found to be quite variable. Peaks for PC-1, used to identify the wavenumbers and corresponding chemical components that differed the most between Sm and PSm coatings, were obtained from the divergence of PCA loading. The intensity of the loading peaks indicates a degree of difference, with higher intensity showing the most variation. The key peaks are highlighted in Figure 3C, and the corresponding biochemical compounds are summarized in Table S2 (Supporting Information). Within the lipid region, two groups of weaker peaks associated with changes to the methyl/methylene groups (2960 and 2925 cm^{-1}) of the phospholipids within the cell membrane were observed. These changes likely result from the rupture of the cell membrane due to plasma treatment. Most of the peaks within the PC-1 loadings are in the amide I and amide II bands, as indicated by the bands at 1638, 1514, and 1452 cm^{-1}. Variations within the polysaccharide regions could be due to alterations in the various structural polysaccharides during plasma treatment, as demonstrated by changes in the 1155 and 1045 cm^{-1} bands. Thus, these results align with previous studies, contributing to our understanding of the effects of Ar-APJ on the functional groups of microalgae (more details can be found in Text S5, Supporting Information).

Likewise, the changes observed in the PCA loading spectra are readily apparent when examining individual spectra extracted from second derivatives (Figure 3D). These alterations are characterized by heightened amide I and II bands in PSm compared

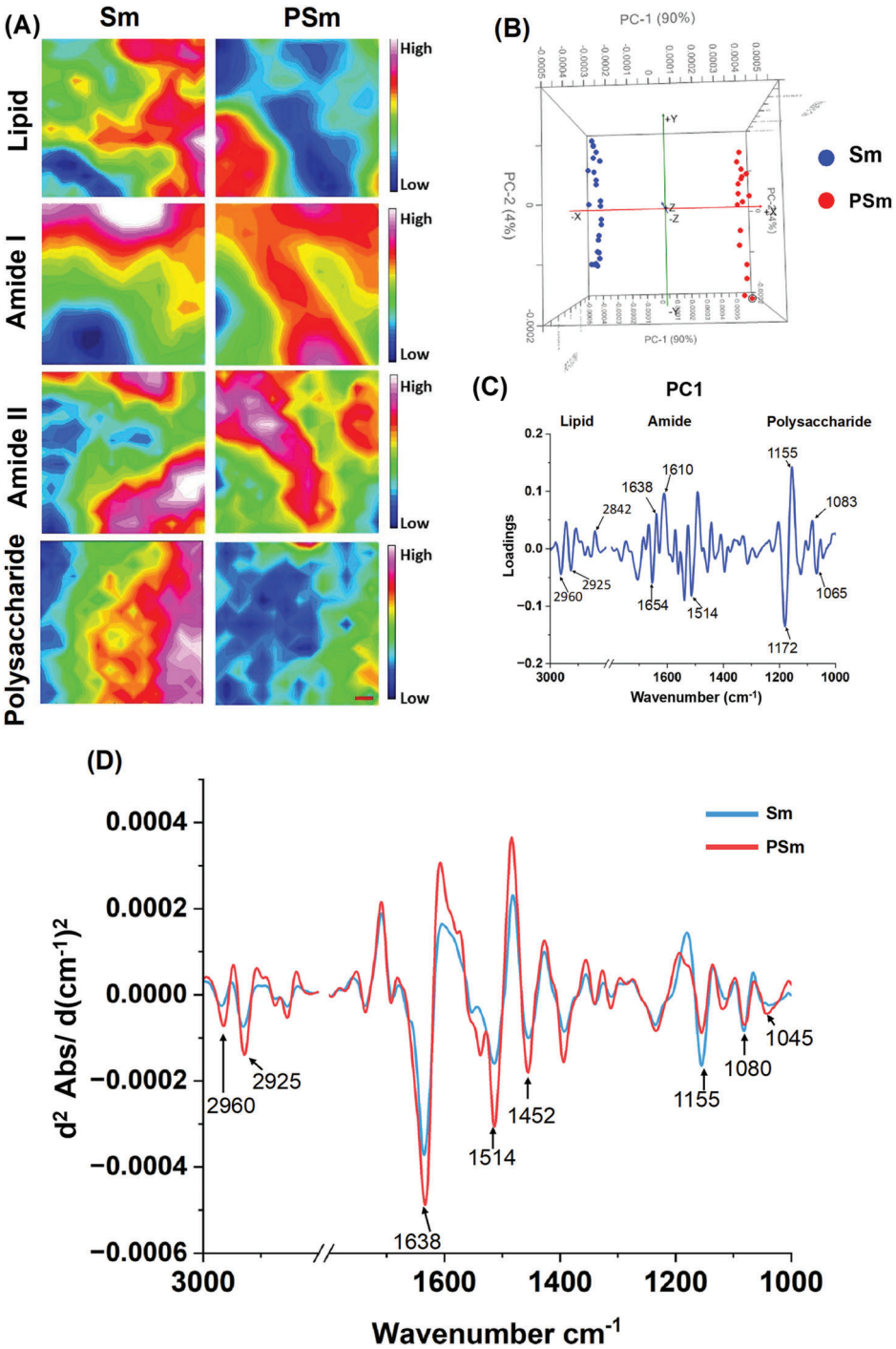

Figure 3. Mapping the biochemical changes of untreated (Sm) and Ar-APJ-treated (PSm) coatings using synchrotron macro attenuated total reflection Fourier-transform infrared (ATR-FTIR) microspectroscopy. A) Heat map images of different chemical components in *S. maxima*, including lipid, amide I/II (protein), and polysaccharide regions across Sm and PSm coatings. Scale bar = 20 µm. B) PCA score plots of Sm and PSm. C) PCA-PC1 loading spectra. D) Second derivative FTIR spectra.

to the Sm coating. Moreover, the amide I band exhibits a subtle broadening and shift, while the amide II band undergoes deformation and a slight shift toward a lower wavenumber after plasma treatment. In the lipid region, the peaks experience a slight shift toward a lower wavenumber, indicating lipid oxidation resulting from the Ar-APJ treatment. However, the most significant variation is observed in the polysaccharide region. Notably, the peak intensity at 1045 cm^{-1} diminishes and exhibits slight broadening, while simultaneously shifting toward a higher wavenumber post-treatment.

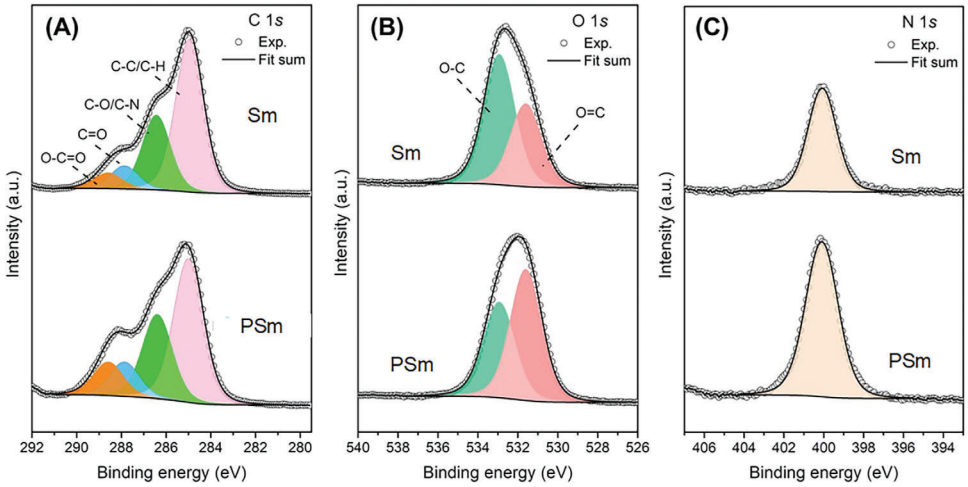

Figure 4. XPS spectra of Sm and PSm in A) C 1s, B) O 1s, and C) N 1s regions.

2.4. Analysis the Elemental Composition and Chemical State of *S. maxima* after Ar-APJ

The effect of Ar-APJ treatment on the chemical composition of *S. maxima* was investigated using X-ray photoelectron spectroscopy (XPS) (**Figure 4**; Figure S3 and Table S3, Supporting Information). The C 1*s*, O 1*s*, and N 1*s* spectra of *S. maxima* before and after plasma treatment are shown in Figure 4. The C 1*s* spectrum in Figure 4A can be deconvoluted into various carbon species, in which the highest peak at 285 eV corresponds to C—H/C—C bonds while the remainder located at ≈286.4, 287.9, and 288.6 eV are assigned to C—O/C—N, C═O, and O—C═O functional groups, respectively.[39,40] Interestingly, the PSm samples exhibit a remarkable decrease in C—H/C—C and C—O/C—N groups but increase in O—C═O groups, indicating a strong interaction between the *S. maxima* samples and ROS generated by the atmospheric plasma. The same trend can also be observed in the O 1*s* spectra with the O═C/O—C ratio increasing from 0.6 for Sm to 1.4 for PSm coatings (Figure 4B and Table S3, Supporting Information). These findings are consistent with the ATR-FTIR analysis discussed above. In addition, the XPS data revealed a higher nitrogen content in the plasma-treated samples (Figure 4C and Table S3, Supporting Information), likely related to the cytoplasmic proteins released by the cell membrane disruption. This is also evident by the significant increase in the amounts of trace elements (e.g., phosphorus, magnesium, potassium, calcium, and sodium) detected in *S. maxima* samples after Ar-APJ treatment (Figure S3 and Table S3, Supporting Information).

2.5. Effects of Ar-APJ Treatment on Bioactive Compounds of *S. maxima*

The effects Ar-APJ treatment on the bioactive components of *S. maxima* were assessed (**Figure 5**A). The total protein and total polysaccharide of Sm and PSm coatings were extracted and quantified as previously described.[41] As expected, PSm had lower total polysaccharide contents in comparison to untreated Sm, shown in Figure 5B, Text S6, and Figure S6 (Supporting Information). These findings suggested that Ar-APJ treatment on *S. maxima* caused a breakdown of some polysaccharides into smaller fragments.[30] The decrease in polysaccharide content in PSm can be attributed to the structural changes caused by the treatment, resulting in near-complete destruction of the cell wall. This interpretation is also supported by the ATR-FTIR and XPS analysis of the polysaccharide spectral region which consistently indicated a reduction in polysaccharide abundance. As a consequence, a larger quantity of bioactive compounds was released. As shown in Figure 5C, the percentage of total protein in the Sm and PSm was measured to be 43.7% and 39.9%, respectively. However, there was no significant difference between these samples ($p > 0.05$), i.e., Ar-APJ treatment did not significantly affect the protein components.

C-phycocyanin is an important bioactive pigment-protein complex of interest in *S. maxima*, and is responsible for antibacterial and antioxidant properties.[42,43] To evaluate the release of C-phycocyanin from *S. maxima*, Sm and PSm coatings were soaked in a phosphate-buffered saline (PBS, 10×10^{-3} M, pH 7.4) solution at 37 °C over 0.25, 1, 24, and 48 h (Figure 5A). The study revealed a consistent increase in C-phycocyanin release for both Sm and PSm. More specially, Sm released 10.3 μg mL^{-1}, while PSm released ≈9.6 μg mL^{-1} of C-phycocyanin at the 15-min mark (Figure 5D). After 48 h, Sm released cumulatively 21.1 μg mL^{-1} of C-phycocyanin, compared to 19.4 μg mL^{-1} for PSm. Notably, PSm consistently exhibited lower levels of C-phycocyanin release compared to Sm at all time points. The formation of a new matrix of polysaccharides after Ar-APJ treatment may contribute to the better retention and slower release of C-phycocyanin. In the context of wound healing applications, the slower release of C-phycocyanin from PSm could be advantageous. A sustained and slower release may allow for prolonged delivery of C-phycocyanin over an extended period, thereby maintaining its anti-inflammatory, antioxidant, and wound-healing properties.[42,43] The availability of C-phycocyanin in PSm for an extended duration could lead to persistent therapeutic effects.

Antioxidants contribute to wound healing by shielding tissues and cells from harmful oxidative species that can impair the

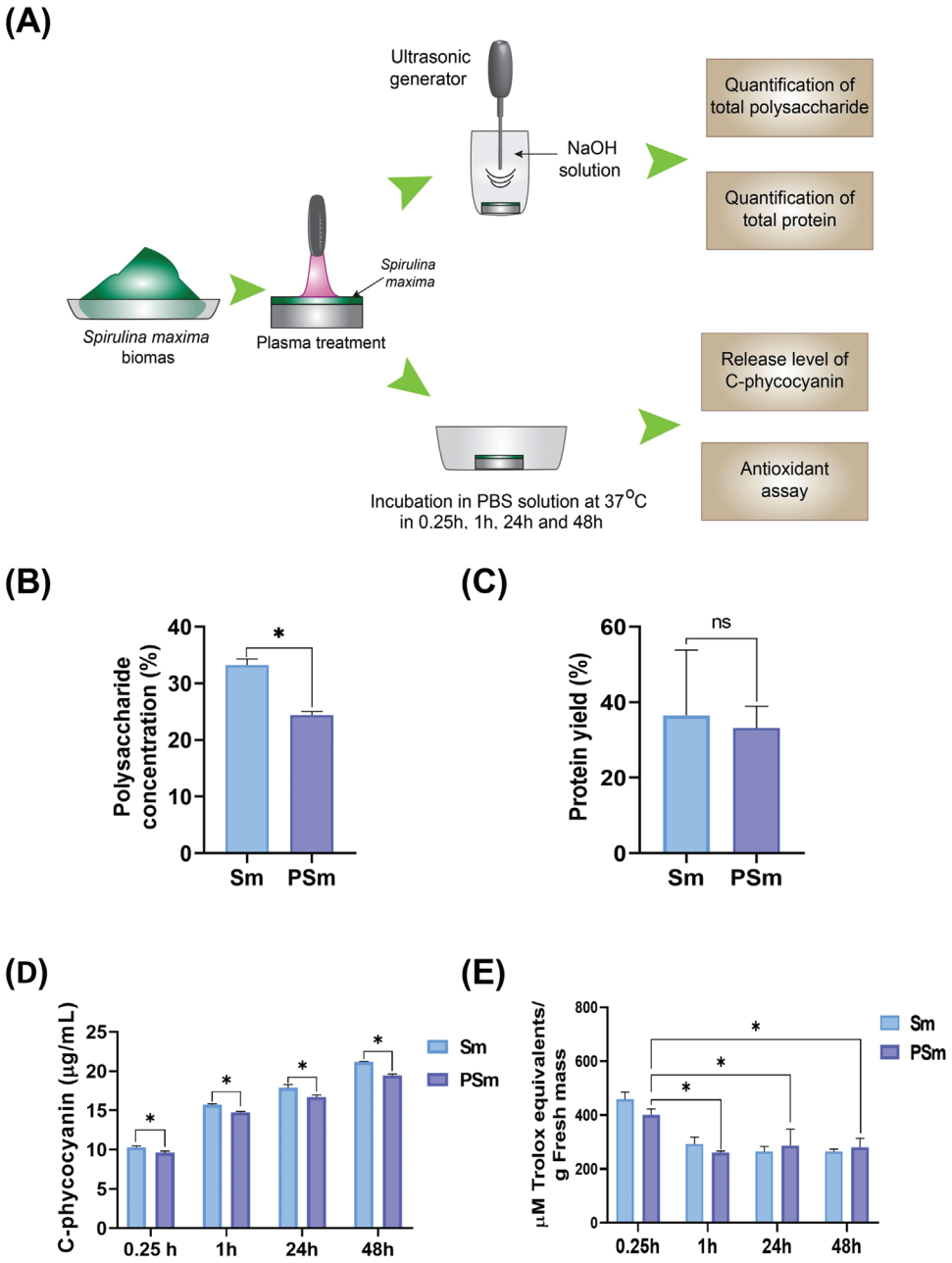

Figure 5. Effects of treatment on bioactive components of *S. maxima*. A) The diagrams showing the process to evaluating bioactive compounds of treated (PSm) and untreated (Sm) *S. maxima*. B) Total polysaccharide concentrations, and C) total protein concentrations of Sm and PSm. D) The concentrations (μg mL^{-1}) of released C-phycocyanin in PBS (10×10^{-3} M, pH 7.4) from the Sm and PSm coatings. E) DPPH assay used to quantify antioxidant activity of these coatings. $n = 3$, all data represented as mean ± SD, $^{*}p < 0.05$, $^{**}p < 0.01$, $^{***}p < 0.001$, $^{****}p < 0.0001$.

healing process.[42,43] As shown in Figure 5E, the antioxidant properties of Sm and PSm coatings were sustained over a 48-h period. We observed a strong antioxidant activity for both Sm and PSm after 15 min (0.25 h). The antioxidant performance remained stable for both coatings after 1 h. At durations greater than 1 h, there was no significant difference in antioxidant performance between the Sm and PSm samples. This indicates that the Ar-APJ process does not interfere with the antioxidant functionality of the bioactive components.

2.6. Antibacterial and Antifouling Capacity of Ar-APJ-Treated *S. maxima*

The antibacterial activity of Sm and PSm was assessed using confocal laser scanning microscopy (CLSM, **Figure 6**). For *Pseudomonas aeruginosa*, both Sm and PSm had a high rate of antibacterial activity, with 82% and 93% dead cells, respectively. Furthermore, qualitative SEM analysis (**Figure 7**A) revealed a reduction in cell density and disruption to typical morphology of

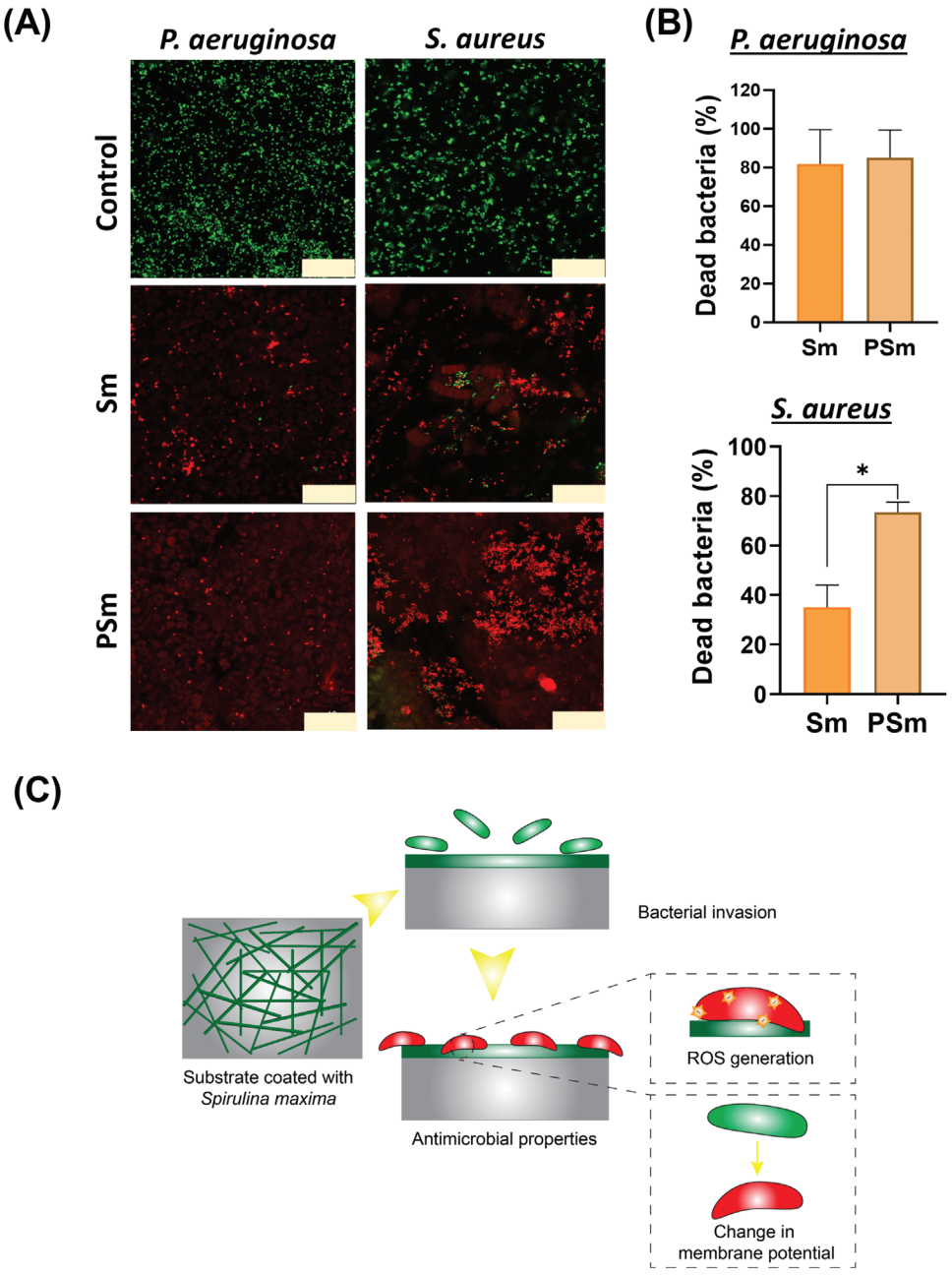

Figure 6. Evaluating antibacterial properties of untreated (Sm) and Ar-APJ-treated *S. maxima* (PSm) against Gram-negative *Pseudomonas aeruginosa* and Gram-positive *Staphylococcus aureus*. A) Confocal laser scanning microscopy (CLSM) images and corresponding plots quantifying the antibacterial efficacy of Sm and PSm against B) *P. aeruginosa* and C) *S. aureus*. Dead bacteria are colored as red, viable bacteria are colored green. Scale bar = 10 µm. $n = 3$, all data represented as mean ± SD. ****$p < 0.0001$. C) Illustrated schematic depicting the antibacterial mechanism of Sm and PSm involving reactive oxygen species (ROS) and membrane potential.

P. aeruginosa. For *Staphylococcus aureus*, the Sm coating had an antibacterial efficacy of 35%, which was increased to 73% on the PSm substrate. This observation was also accompanied by an observation of reduced cell density.

To elucidate the capacity of Sm and PSm to inhibit biofilm formation, we cultured *S. aureus* and *P. aeruginosa* on the substrates for 48 h and measured biofilm thickness, biovolume, and absorbance of safranin (**Figure 8**). We observed significant reductions in all metrics for Sm and PSm coated surfaces, compared to the untreated control substrate. The biovolume of *S. aureus* and *P. aeruginosa* was reduced by 70%–80% on the Sm and PSm substrates compared to the untreated control substrates. The biofilm thickness of *S. aureus* was reduced by 55%–60% on the Sm and PSm substrates, while for *P. aeruginosa*, the reduction was 75% in the case of PSm. These results were corroborated by a safranin absorbance assay, which measured a decreased absorbance by

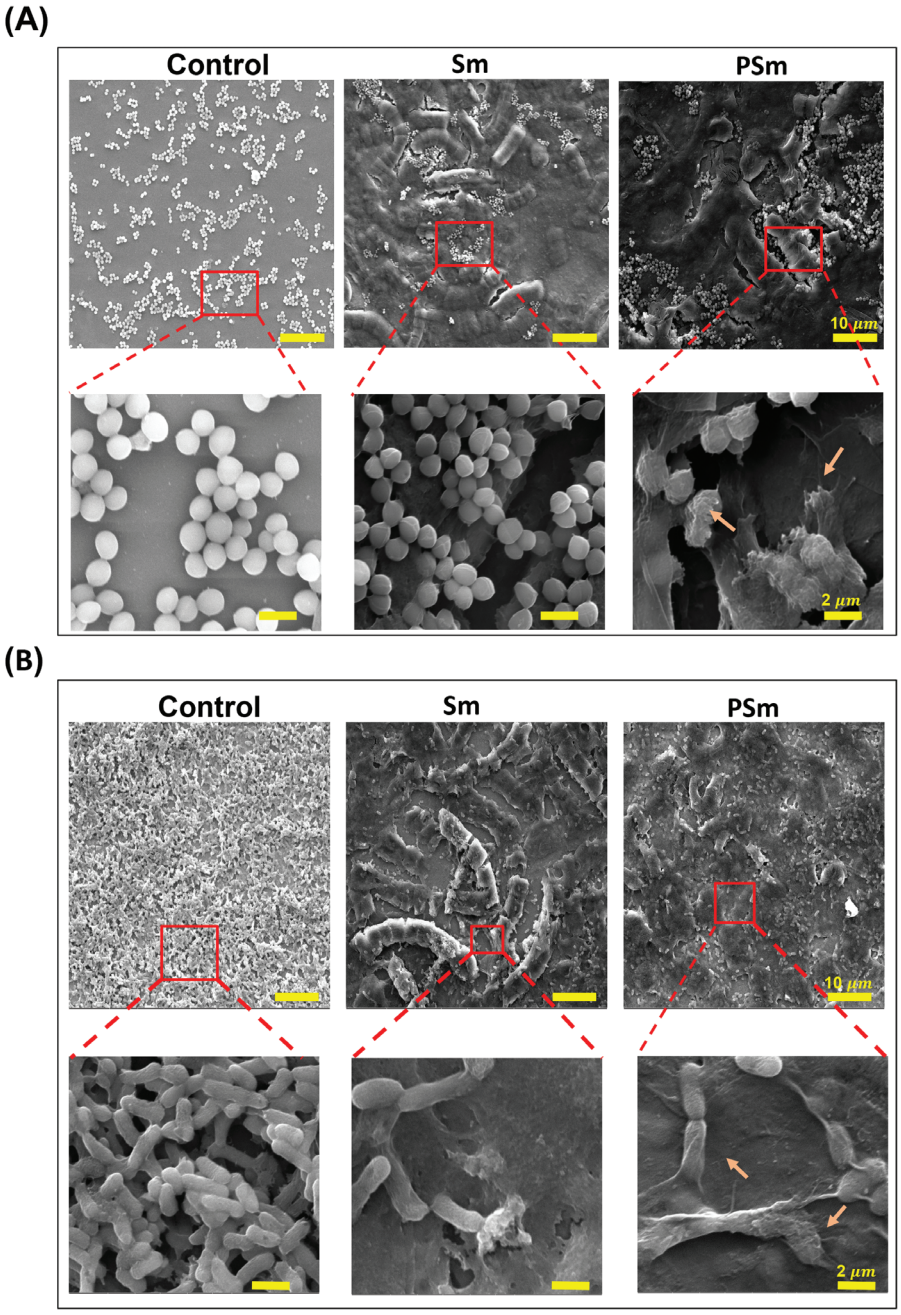

Figure 7. SEM images showing the morphology of A) *P. aeruginosa* and B) *S. aureus* on Sm and PSm. Scale bar (top row) = 10 µm, scale bar (inset - bottom row) = 2 µm.

≈50% for *S. aureus* and ≈78%–80% for *P. aeruginosa* on both substrates. These results confirm that the bactericidal activity of Sm and PSm surfaces inhibits the formation of biofilm.

2.7. Examining Antibacterial Mechanisms of Both Sm and PSm Coatings

The fluorescence intensity analyzed via CLSM was utilized to assess the membrane potential and intracellular ROS of both *P. aeruginosa* and *S. aureus* on Sm and PSm. The results, shown in **Figure 9** demonstrate that more ROS were formed for both *P. aeruginosa* and *S. aureus* on PSm compared to Sm. This aligns with previous research which has shown that antimicrobial compounds can lead to the intracellular generation of ROS, imposing secondary bactericidal effects beyond the primary target mechanism of the antimicrobial compound.[44] This process is thought to occur via the overstimulation of electrons via the tricarboxylic acid cycle, the activation of Fenton chemistry. Therefore, the higher ROS generation on PSm compared to Sm could be

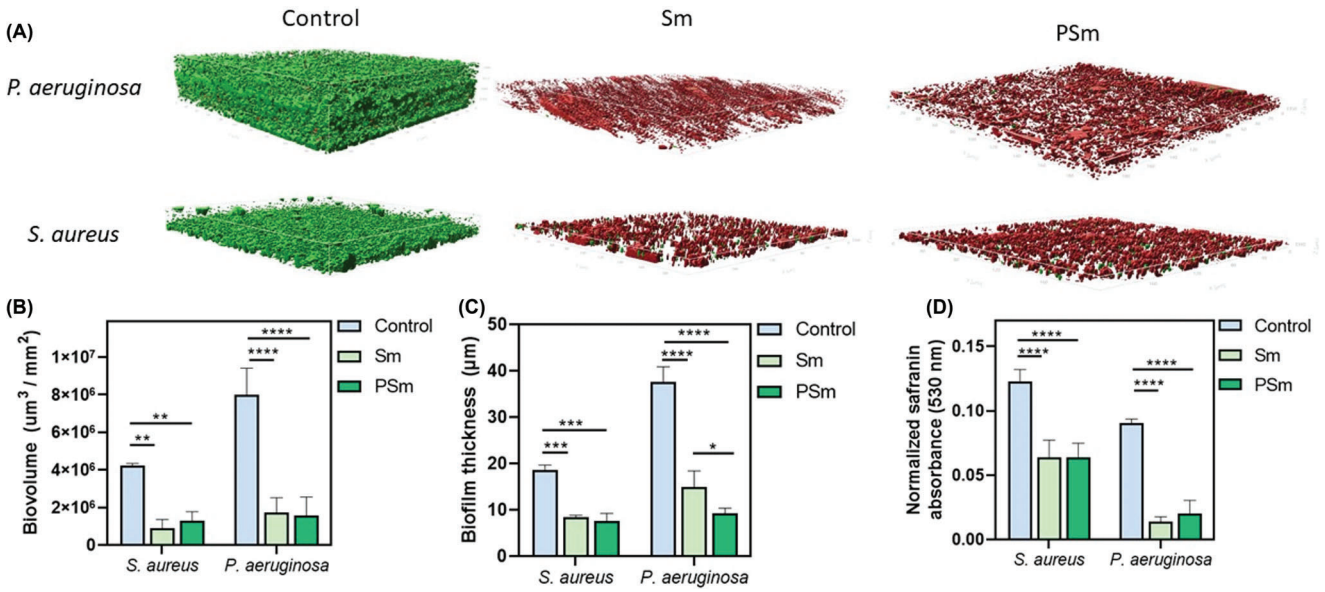

Figure 8. The antifouling capacity of Sm and PSm against *S. aureus* and *P. aeruginosa*. A) 3D model representations of Z-stack micrographs captured by CLSM. B) Biovolume measurements. C) Biofilm thickness. D) Safranin absorbance study. $n = 3$, all data represented as mean ± SD, $*p < 0.05$, $**p < 0.01$, $***p < 0.001$, $****p < 0.0001$.

attributed to this mechanism. Indeed, the intracellular generation of ROS has been proposed as a common end-point in the bactericidal mechanism of multiple antimicrobials with differing primary targets,[45] making it plausible that a similar occurrence is observed with Sm and PSm. Figure 9 further reinforces this observation, showing a lower ratio of polarized to depolarized membrane for both *P. aeruginosa* and *S. aureus* on PSm compared to Sm. This indicates that there is more membrane damage on PSm and points to the major antibacterial mechanism being the production of intracellular ROS, leading to cell death.

2.8. Biocompatibility Assay

We further evaluated the biocompatibility of untreated (Sm) and treated (PSm) *S. maxima* coatings. Macrophages grown from differentiated THP-1 monocytes were selected as the *in vitro* cellular model.[46] A standard MTT assay which measures the metabolic activity of cells was used to determine cell viability. No significant reduction in cell viability was noted for either Sm or PSm for 24 h (**Figure 10**A). The THP-1 cells proliferated to full confluency after 72 h on PSm. The CLSM micrographs of THP-1 cells (stained with DAPI and phalloidin) on both Sm and PSm in Figure 10A demonstrate that the cells adopted their normal metabolically active morphology. The cells appear to be more proliferated on PSm compared to Sm. Based on these results, Sm and PSm were safe and do not possess any cytotoxicity, according to ISO 109993-5 standards.[47] These results were consistent with previous literature, which indicated that *S. maxima* is safe for use with human cells.[48]

We also evaluated the pro-inflammatory response of THP-1 macrophage to Sm and PSm by measuring the secretion of IL-6. IL-6 is a pro-inflammatory cytokine crucial in chronic inflammatory diseases. It is produced by cells such as macrophages, T-cells, and B-cells, participating in the immune response against infections and tissue damage.[49] The concentrations of IL-6 were measured at two different time points as shown in Figure 10C. More detailed information is presented in Text S7 (Supporting Information). After 1 d of incubation, IL-6 levels on Sm and PSm were detected to be 172.3 and 112.6 pg mL^{-1} of IL-6, respectively. And after 3 d of incubation, the concentration of IL-6 secreted by THP-1 cells on PSm was significantly lower than that of Sm. This indicates that PSm coatings exhibit superior anti-inflammatory properties, which may be beneficial for wound healing.

2.9. Keratinocyte Proliferation and Wound Scratch Assay

The impact of Sm and PSm coatings on mammalian cell proliferation was investigated using HaCaT cells as a model skin cell line. CLSM micrographs (**Figure 11**A) showed qualitatively that HaCaT cell density was comparable on all tested surfaces after 3 d of incubation. Furthermore, the MTT assay revealed that there was no significant difference in HaCaT viability between the Sm and PSm surfaces (Figure 11B).

Keratinocyte migration plays a pivotal role in wound closure and re-epithelialization. The ability of Sm and PSm to promote the migration of human epidermal keratinocytes (HaCaT) was investigated using wound scratch assay.[50] The scratch width, as defined by the distance between the edges of the scratch, of Sm and Psm were 789 ± 18 and 236 ± 17 µm, respectively, on day 1. On day 2, the wound was completely closed on PSm, whereas, the wound scratch was still open in the case of Sm and control. The scratch widths between different groups and time points showed statistically significant differences, clearly demonstrating the better healing ability of PSm compared to Sm. The results indicate that on the PSm coatings the cells exhibited significantly higher migration levels than on Sm and control after 2 d. This is in

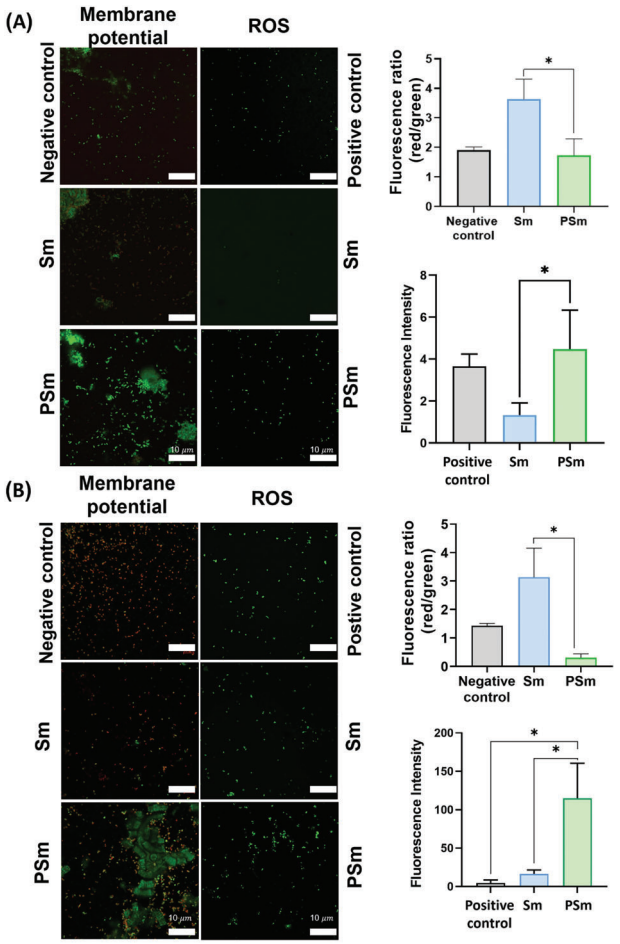

Figure 9. Membrane potential and intracellular ROS generation. A) CLSM micrographs and ratio of polarized to depolarized membrane and fluorescence intensity of ROS created when incubated *P. aeruginosa* with Sm and PSm. Green signal in CLSM micrographs represents intracellular ROS. B) CLSM images and ratio of polarized and depolarized membrane and fluorescence intensity of ROS created when incubated *S. aureus* with Sm and PSm. Green and red presented bacterial with polarized and depolarized membrane, relatively. Scale bar = 10 µm. $n = 3$, all data represented as mean ± SD, $^{*}p < 0.05$, $^{**}p < 0.01$, $^{***}p < 0.001$, $^{****}p < 0.0001$.

agreement with the MTT results. The capacity of the PSm coatings to enhance skin cells migration is a valuable property, indicating potential for enhancing wound healing rate.

Overall, our investigations into the antibacterial, antifouling, biocompatibility, and wound healing properties of PSm reveal that the materials generated by our process possess dual functionality. As bacterial infections are a primary factor in poor wound healing, the PSm coatings promise to improve clinical outcomes by simultaneously inhibiting bacteria and promoting wound healing.

3. Conclusion

We have developed a novel Ar-APJ process which can transform *S. maxima* biomass into a bioactive ultrathin coating for treating wound infections and enhancing wound healing. We found that our Ar-APJ system is sufficiently delicate to break down cell walls of microalgae while enabling the retention of most of bioactive components of *S. maxima*. Subsequently, the fragmented cell wall was reformed to create a contiguous layer which acts as a robust and stable ultrathin coating. This treatment promoted the sustained release of bioactive compounds such as C-phytocyanin. The Ar-APJ assisted coating was found to exhibit enhanced antimicrobial properties compared to the already high antibacterial rate of untreated *S. maxima*. Ar-APJ-assisted coating was found to be biocompatible with THP-1 and HaCaT cells. Furthermore, a reduction in the expression of pro-inflammatory cytokines suggests a favorable reduction of inflammation. The results presented herein provide support for the potential wound healing properties of Ar-APJ-assisted *S. maxima* coating, attributed to its diverse bioactive components. However, it is important to note that other components in *S. maxima* may also contribute to these effects, warranting further advanced experiments to elucidate the underlying phenomena. Overall, this study demonstrates the potential of our Ar-APJ technology to generate bioactive coating from *S. maxima* and thus overcome current processing challenges.

4. Experimental Section

Integrated Plasma System for the Treatment of Microalgae Biomass: The configuration of the integrated atmospheric plasma jet system for the treatment of microalgae biomass was set up as shown in **Figure 12**A. AC power supply (Variac SRV-5, POWERTECH, AU) was employed in conjunction with an electronic transformer (NP-10000-30, NeonPro Co, USA) to power the jet system. The power supply maintained a fixed frequency of 24 kHz, while the voltage was set to 10 kV. A tungsten-steel rod (150.0 mm × 2.5 mm) inserted into a dielectric ceramic tube (150 mm length, inner diameter 12.0 mm, outer diameter 14.0 mm) was connected to the high-voltage power supply, while a cone-shaped grounded electrode was positioned at a distance of 15 mm from the nozzle. To prevent the plasma from turning into an arc discharge, a 10 kΩ resistor was installed. The plasma jet was ignited directly from the nozzle, which was located 30 mm above the samples (Figure 12B), with argon gas supplied at a flow rate of 10.0 standard LPM. More information was included in Text S1 (Supporting Information). A PLASUS EMICON MC spectroscopic plasma monitor and process control system (PLASUS, DE) with EMICON MC version 4.6 software was used to record the optical emission spectroscopy[11] of argon plasmas. The optical sensor head was positioned at a distance of 250 mm from the plasma jet (see Figure 12).

Sources of S. maxima: *S. maxima* (OxyMin Spirulina Organic) was obtained as the dry biomass from OxyMins (QLD, Australia). Most of these cells were found to be nonviable. The compositions of *S. maxima* are shown in Figure S6 (Supporting Information).

Effects of Ar-APJ Treatment on Morphology of S. maxima Cell: Prior the plasma treatment, microalgae *S. maxima* was coated on various surfaces (silicon wafers, coverslips, and glass slides) to achieve the dry weight density of 0.1 mg cm^{-2}. More details are explained in Text S8 (Supporting Information). Then, it was treated with atmospheric plasma in 100 and 200 s cm^{-2}. The glass slides were stained for 5 min with a 0.01% calcofluor white solution (Sigma-Aldrich, Inc., Saint Louis, MO), and potassium hydroxide was added to improve sensitivity in detecting microalgae. The image of *S. maxima* cell wall with and without treating plasma was observed by Olympus IX83 inverted epifluorescence microscope.[51] Prior to scanning electron microscopy, the microalgae were coated with 2 nm platinum. Scanning electron microscopy was performed at Flinders Microscopy and Microanalysis using an FEI Inspect F50 SEM (https://doi.org/10.25957/flinders.sem). Electron micrographs were obtained with an electron beam voltage of 5 kV.

Sessile Drop Water Contact Angle Measurements: Sample wettability was studied using a RD-SDM02 contact angle measuring equipment. Sm

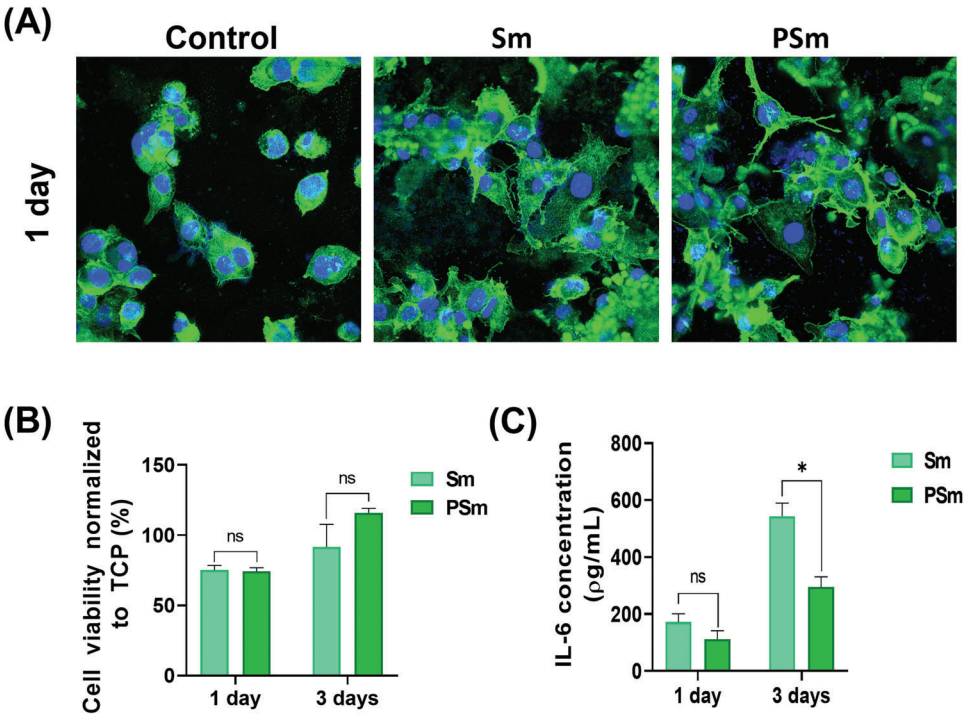

Figure 10. Evaluation of biocompatibility of Sm and PSm against THP-1 macrophage. A) CLSM images of THP-1 macrophage cell in 1 d after incubating on Sm and PSm substrates. B) Viability percentage normalized to tissue culturing plates (TCP) of THP-1 cell after incubating with Sm and Psm substrates for 1 and 3 d. C) IL-6 concentration of THP-1 (pg mL^{-1}) after incubating with Sm and PSm for 1 and 3 d. $n = 3$, all data represented as mean ± SD, $^{*}p < 0.01$.

and PSm samples with concentration 0.6 and 0.1 mg cm^{-2} deposited on round glass coverslips were used as substrates for the wettability measurements. Small droplet of 3 µL Milli-Q water was carefully placed on the surface to determine the advancing contact angle. Subsequently, the droplet's images were captured using a microscope camera and was used to measure using ImageJ.

Synchrotron ATR-FTIR Microspectroscopy: The setup was carried out previously.[38] A single FTIR image covering a 350 × 350 mm^2 sampling area was captured using an Agilent FTIR microscope equipped with a liquid-N_2 cooled Stingray FPA detector and a 15× objective lens. Each FTIR image was made up of a 32 × 32 array of spectra that represented chemical data that was collected from a region on the sample plane that was around 10.9 × 10.9 mm^2. For each biological replication, Resolution Pro was used to get at least five excellent FTIR spectral map. Prior to each sample spectral image measurement, IR imaging software with an 8 cm^{-1} resolution, 128 co-added scans, and background measurements were carried out.

XPS Analysis: A Thermo Scientific K-alpha XPS spectrometer equipped with Al Kα X-ray source (1486.7 eV) and concentric hemispherical electron analyzer was utilized for XPS experiments. All *S. maxima* samples were prepared on silicon substrates. The XPS data were then analyzed with CasaXPS software. C 1s peak at 285 eV was used as a charge reference.[40,52] To minimize possible damages to the samples caused by prolonged X-ray exposure, XPS was carried out in the multiplex mode with seven scans for each element and two scans for XPS survey.

Phytochemical Compounds: Sm and PSm coatings were incubated with 50 mL of 0.5 M NaOH/urea solvent. The mixture was placed into an ultrasonication apparatus (Sonics VibraCell VXC 500) at frequency of 40 kHz and power of 80 W. The ultrasonication treatment was carried out continuously at room temperature for 30 min. After that, solution was centrifuged 10 000 rpm in 10 min to collect supernatant. This supernatant was used for examining total polysaccharide and protein concentration. The total polysaccharide content was assessed using the phenol/acid sulfuric acid method,[53] while the total protein content was determined using the Lowry method[54] content. Further details can be found in Text S9 (Supporting Information).

Release Level of C-Phycocyanin: *S. maxima* solution was sprayed onto a 12-well plate to achieve a density of 0.1 mg cm^{-2}. Atmospheric plasma jet treatment was then applied to the plate surface as above. Next, 1 mL of PBS (pH = 7.4) was added to each well and incubated at 37 °C in the dark. The release level of C-phycocyanin was evaluated at various time points, including 15 min, 60 min, 24 h, and 48 h. Cell debris was removed from the PBS solution through centrifugation at 13 000 rpm for 10 min, and the blue-colored supernatant was collected. The supernatant was then analyzed at wavelengths of 615 and 652 nm using SYNERGY-HTX multiwell plate reader. C-phycocyanin concentration was determined by applying equation below.[55]

$$\text{C} - \text{phycocyanin}\ \ (\text{mg/mL}) = \frac{\text{OD}_{615} - 0.474 \times \text{OD}_{652}}{5.73} \tag{7}$$

Antioxidant Ability: The 2,2-diphenyl-1-picrylhydrazyl (DPPH) assay was conducted following the previous method.[56] A stock solution was prepared by dissolving 24 mg of DPPH in 100 mL of methanol, which was then stored at −20 °C until further use. The working solution was prepared by mixing 10 mL of the stock solution with 45 mL of methanol to achieve an absorbance at 515 nm using a SYNERGY-HTX multiwell plate reader (BioTek, Vermont, USA). The sample (150 mL) was then allowed to react with 2850 mL of the DPPH solution in the dark for 24 h. Subsequently, the absorbance was measured at 515 nm. The standard curve was found to be linear in the concentration range of 25–800 × 10^{-3} M Trolox. The results were expressed in mM Trolox equivalent/g fresh mass (TE/g). Additional dilution was performed if the measured DPPH value exceeded the linear range of the standard curve.

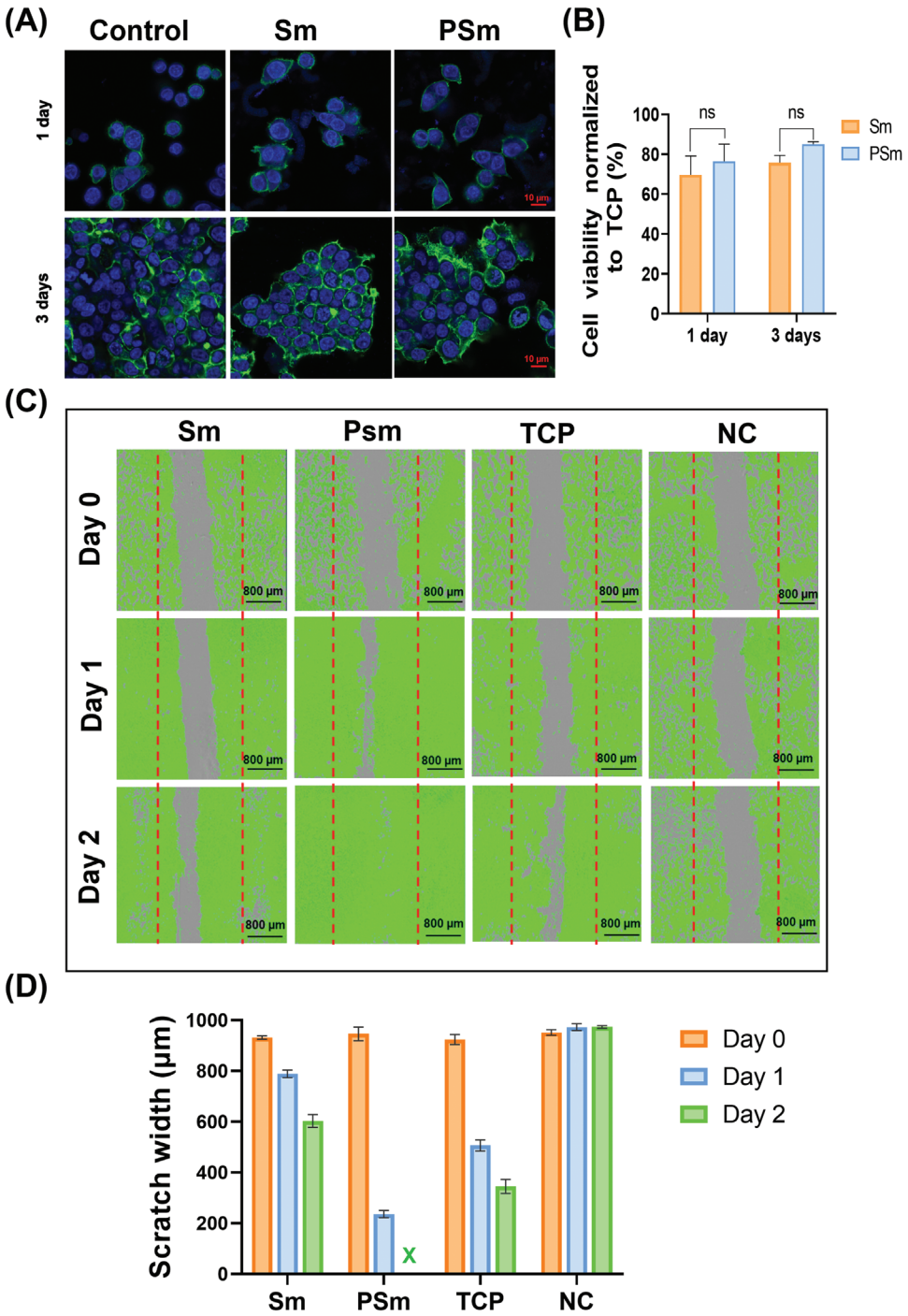

Figure 11. Evaluating the wound healing ability of Sm and PSm. A) CLSM images of HaCaT cell (blue shows nucleus stained with DAPI, and green shows F-actin stained with phalloidin) over the periods of 1 and 3 d, scale bar = 10 μm. B) Viability normalized to tissue culture plates (TCP) of HaCaT cell after incubating with Sm and PSm in 1 and 3 d. C) Wound scratch assay using HaCaT cells after incubation with Sm, PSm, TCP, and negative control (NC) from day 0 to day 2. D) Scratch width of HaCaT cell after incubating with Sm and PSm (Green X menas complete healing or wound closure). Scale bar = 100 μm. $n = 3$, all data represented as mean ± SD, $^*p < 0.001$.

Standard curve of antioxidant ability was presented in Text S7 (Supporting Information).

Evaluating Antibacterial Capacity: The Sm and PSm coatings were placed in a 12-well tissue culture plate and then seeded with 200 μL of *S. aureus* ATCC 25923 *and P. aeruginosa* ATCC 15692 at a concentration of 10^5 CFU mL^{-1}. After the silicon wafer was incubated for 18 hours, it was gently washed once with PBS. Next, the bacteria were stained for 10 min in SYTO9 (Sigma) (excitation and emission maxima, 480 and 500 nm) and propidium iodide (PI) (Sigma, excitation, and emission, 490 and 635 nm) in the ratio of 1:1. Confocal laser scanning microscope (Zeiss_LSM880,

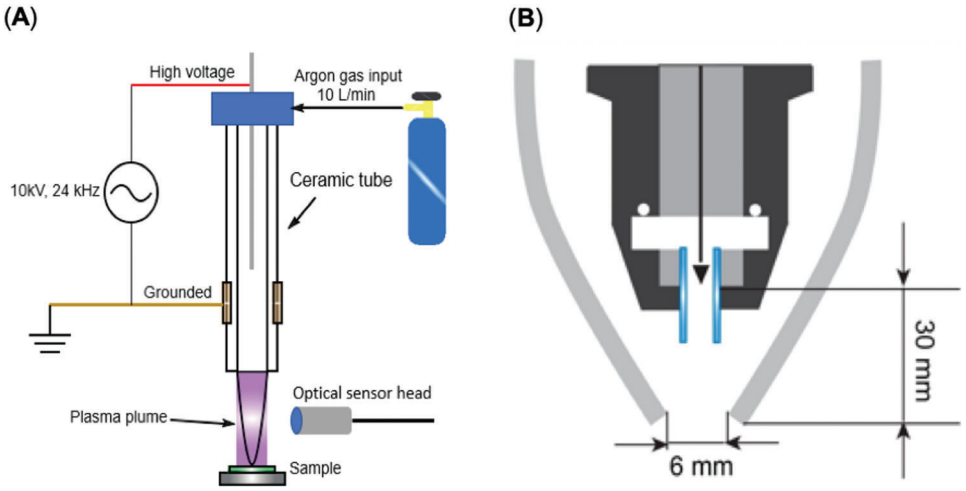

Figure 12. Schematics showing the setup of Ar-AAJ. A) Schematic representation of the integrated plasma jet system with the optical emission spectroscopy characterization systems; and B) the outlet design of the plasma jet reactor.

Oberkochen, Germany) was used to observe the percentage of dead bacteria.

$$\text{Antibacterial percentage} = \frac{\textit{Dead bacterial}}{\textit{Total bacterial}} \times 100\% \quad (8)$$

The bacterial cells were fixed in 4% glutaraldehyde for 1 h at room temperature. The samples were dehydrated in a sequential graded ethanol (30%, 50%, 70%, 90%, and 100%). Finally, all samples were coated with 2 nm platinum. Samples were then observed in a FEI Inspect F50 (FEI Company, Oregon, USA) at 5 kV with a working distance of 5 mm.

ROS Quantification: To initiate the assay, 100 µL of the diluted 2′,7′-dichlorofluorescin diacetate (DCF-DA) solution (Abcam, Australia) was added to each well. The plate was then incubated for 45 min at 37 °C in a dark environment. Subsequently, the DCF-DA solution was carefully removed from the wells. As a positive control, *tert*-butyl hydroperoxide (TBHP) was applied to the bacterial samples without *S. maxima*. The fluorescence measurements were conducted using CLSM at an excitation/emission wavelength of 485/535 nm. The fluorescence intensity was used to determine the density of ROS.

$$\text{Fluorescence intensity} = FI_{test} - FI_{blank} \quad (9)$$

where FI_{test} represented fluorescence of green color of Sm and PSm and FI_{blank} represented fluorescence intensity of background.

Membrane Integrity Quantification: Bacteria on Sm and PSm were stained with 1×10^{-6} M DiO (Biotium Corp., Hayward, CA) and incubated in the dark for 5 min. Then, 2×10^{-6} M DPA was added to the bacterial solution and incubated for 45 min in the dark. Finally, fluorescence images were captured using CLSM.[57]

$$\text{Ratio of polarized and depolarized membrane} = \frac{FI_{red}}{FI_{green}} \quad (10)$$

where FI_{red} represented fluorescence intensity of polarized membrane and FI_{green} represented green fluorescence intensity of depolarized membrane.

Biofilm Culture: A single colony of *S. aureus* ATCC 25923 and *P. aeruginosa* PAO1 was transferred to 5 mL of tryptone soy broth (TSB) and incubated overnight at 37 °C until stationary phase. The cell density was inferred from optical density at 600 nm and the overnight culture was diluted to a final cell density of 10^6 CFU mL^{-1}. The treated and untreated substrates were placed in 24-well plates and sterilized by UV exposure for 20 min per side. The sterile substrates were immersed in 1 mL of bacterial cell suspension and then stored in a sealed box with a damp paper towel to maintain a humid environment. The box was placed atop an orbital shaker at 60 RPM in a warm room (37 °C) for 48 h. After the first 24 h, the cell suspension in each well was replaced with fresh media to remove exhausted nutrients and stationary phase cells.

3D Biovolume Analysis: The inoculated substrates were gently removed from their cell suspensions and dipped in sterile PBS to rinse off nonadherent cells. The washed substrates were placed in fresh 24-well plates and immersed in BacLight Live/Dead reagents, with an equal proportion of SYTO9 (excitation and emission maxima, 480 and 500 nm) and propidium iodide (excitation and emission maxima, 490 and 635 nm) in PBS at the concentraion of 1.5 µL/mL. The samples were incubated at room temperature for 15 min and then imaged on an Olympus FV3000 confocal laser scanning microscope. At 3 random locations per sample, 3D Z-stack images were assembled by taking scans at 0.5 µm intervals along the Z-axis. The Z-stacks were imported into Imaris 3D analysis software and converted to 3D models using the "surfaces" function. Total biovolume was measured by combining the red and green channels.

Safranin Absorbance: Biofilms were cultured on the substrates as described above. Following incubation, the substrates were gently rinsed in PBS to remove nonadherent cells. Each sample was individually placed in the wells of a clean 24-well plate and immersed in 0.1% safranin for 10 min. The safranin solution was removed and gently rinsed off with sterile PBS. The rinse was repeated two times. PBS was removed and the samples were then immersed in a decolorizing solution of ethanol and acetone at a 1:1 ratio. The samples were left to soak in the decolorizing solution for 10 min on an orbital shaker at 60 RPM. To measure the intensity of absorbance, 100 µL aliquots were taken from the samples and transferred to a 96-well plate and optical density was measured at 530 nm. The *S. maxima* surface coating was expected to contribute to the absorption of safranin, so a Sm and PSm control was used without the presence of bacteria. The absorbance values of the Sm and PSm experimental samples were corrected by subtracting out the value derived from the no-bacteria control.

Biocompatibility and Pro-Inflammatory Assay: Macrophages-like THP-1 cell at a density of 10^5 cells /well were seeded on Sm and PSm coatings. After 24 and 72 h, cytotoxicity assays were performed using MTT assay from Sigma (Text S10, Supporting Information). Macrophage-like THP-1 cells were fixed with 4% paraformaldehyde for 20 minutes. The coatings were then incubated with 0.1% Triton-X (Sigma) for 10 min. Next, it was incubated with Alexa 488-phalloidin (Thermo Scientific) for 90 min. Subsequently, DAPI (Thermo Scientific) was applied and incubated for 10 min. The coatings were then washed with 2 mL of PBS afterward. CLSM was

used to image both phalloidin and DAPI stained samples. Further details can be found in Text S10 (Supporting Information).

The media from each well was collected, followed by stimulation with IL-6. The IL-6 produced in the culture medium was quantified using the IL-6 specific ELISA kit, following the manufacturer's instructions (Invitrogen, Thermo Fisher Scientific, AU). Media without cells was used as a control.[58] More information can be found in Text S11 (Supporting Information).

HaCaT Cell Proliferation: The HaCaT cells (human epidermal keratinocyte line, cell line services, Eppelheim, Germany) were cultured in Dulbecco's Modified Eagle's Medium (DMEM) supplemented with 10% heat-inactivated fetal bovine serum (FBS, Gibco, AU) and 1% streptomycin/penicillin (Gibco-BRL, AU). When the cells reached ≈80%–85% confluence, they were harvested using 0.25% Trypsin-EDTA (1X) (Gibco-BRL, AU). A volume of 200 µL of HaCaT cells at a density of 10^5 cells mL^{-1} was seeded onto Sm and PSm substrates and incubated for 1 and 3 d. MTT and CLSM assays were carried out on HaCaT cells.

Wound Scratch Assay: Wound scratch experiment was conducted using Incucyte SX5 live-cell analysis instrument (Sartorius). Plasma treated and untreated 24-well plates were seeded with 1×10^6 HaCaT cells in triplicates and incubated for 24 h at 37 °C and 5% CO_2 till a uniform cell monolayer was formed. These monolayers were consistently scratched using a sterile 100 µL pipette, washed with 1× PBS and replaced with fresh DMEM. The well plates were placed in Incucyte SX5 live-cell analysis instrument and images were recorded for 2 d. Incucyte 2022A Rev1 software was used to measure the scratch width. The controls involved untreated tissue culture plates (TCP) seeded with cells and the negative control involved cells whose migration were retarded by treating with 1% dimethyl sulfoxide, Sigma (NC).

Statistical Analysis: All experiments were conducted in triplicate to ensure accuracy. The cell viability percentage and all other quantitative data are reported as the mean ± standard deviations . Statistical comparisons were made using ANOVA analysis, with *p*-values less than 0.05 deemed to be statistically significant. The statistical analysis was facilitated using GraphPad Prism version 5.00 for Windows, provided by GraphPad Software, San Diego, CA (www.graphpad.com).

Supporting Information

Supporting Information is available from the Wiley Online Library or from the author.

Acknowledgements

T.P. and T.T.N. contributed equally to this work. K.V. thanks NHMRC for Fellowship GNT1194466 and ARC for grant DP220103543. V.K.T. thanks for the support from Flinders Foundation Health Seed Grant. The authors acknowledge the facilities and the scientific and technical assistance of Microscopy Australia and the Australian National Fabrication Facility (ANFF) under the National Collaborative Research Infrastructure Strategy, at the South Australian Regional Facility, Flinders Microscopy and Microanalysis, Flinders University. The authors would like to thank the RMIT Microscopy and Microanalysis Facility (RMMF). This research was undertaken on the IR microspectroscopy beamline at the Australian Synchrotron, part of ANSTO.

Open access publishing facilitated by Flinders University, as part of the Wiley - Flinders University agreement via the Council of Australian University Librarians.

Conflict of Interest

The authors declare no conflict of interest.

Data Availability Statement

The data that support the findings of this study are available from the corresponding author upon reasonable request.

Keywords

antibacterial, atmospheric plasma jet, bioactive coatings, Spirulina maxima, wound healing, wound infection

Received: June 30, 2023
Revised: August 21, 2023
Published online:

[1] D. J. Anderson, K. Podgorny, S. I. Berríos-Torres, D. W. Bratzler, E. P. Dellinger, L. Greene, A. C. Nyquist, L. Saiman, D. S. Yokoe, L. L. Maragakis, K. S. Kaye, *Infect. Control Hosp. Epidemiol.* **2014**, *35*, 605.
[2] J. Hurlow, P. G. Bowler, *J. Wound Care* **2022**, *31*, 436.
[3] V. Falanga, R. R. Isseroff, A. M. Soulika, M. Romanelli, D. Margolis, S. Kapp, M. Granick, K. Harding, *Nat. Rev. Dis. Primers* **2022**, *8*, 50.
[4] C. K. Sen, *Adv. Wound Care* **2019**, *8*, 39.
[5] D. Voegeli, *Factors that Exacerbate Skin Breakdown and Ulceration*, **2007**, pp. 17–21.
[6] M. Stracy, O. Snitser, I. Yelin, Y. Amer, M. Parizade, R. Katz, G. Rimler, T. Wolf, E. Herzel, G. Koren, *Science* **2022**, *375*, 889.
[7] S. Taheri, A. Cavallaro, S. N. Christo, L. E. Smith, P. Majewski, M. Barton, J. D. Hayball, K. Vasilev, *Biomaterials* **2014**, *35*, 4601.
[8] H. Haidari, S. Garg, K. Vasilev, Z. Kopecki, A. J. Cowin, *Wound Pract. Res.* **2020**, *28*, 173.
[9] N. Ninan, N. Goswami, K. Vasilev, *Nanomaterials* **2020**, *10*, 967.
[10] C. Brouillard, A. C. Bursztejn, C. Latarche, J. F. Cuny, F. Truchetet, J. P. Goullé, J. L. Schmutz, *J. Eur. Acad. Dermatol. Venereol.* **2018**, *32*, 2295.
[11] N. Hadrup, A. K. Sharma, K. Loeschner, *Regul. Toxicol. Pharmacol.* **2018**, *98*, 257.
[12] S. Silver, L. T. Phung, G. Silver, *J. Ind. Microbiol. Biotechnol.* **2006**, *33*, 627.
[13] S. L. Percival, P. G. Bowler, D. Russell, *J. Hosp. Infect.* **2005**, *60*, 1.
[14] A. Ebrahimi, M. Reza Farahpour, S. Amjadi, M. Mohammadi, H. Hamishehkar, *Int. J. Pharm.* **2023**, *630*, 122457.
[15] I. K. Ikeda, E. B. Sydney, A. C. N. Sydney, *J. Cosmet. Dermatol.* **2022**, *21*, 4205.
[16] A. Bitam, O. Aissaoui, in *Diabetes*, 2nd ed. (Ed: V. R. Preedy), Academic, San Diego, CA **2020**, pp. 325–331.
[17] W. Chen, J. Xu, Q. Yu, Z. Yuan, X. Kong, Y. Sun, Z. Wang, X. Zhuang, Y. Zhang, Y. Guo, *Bioresour. Technol.* **2020**, *300*, 122628.
[18] W. Y. Choi, H. Y. Lee, *Int. J. Mol. Sci.* **2018**, *19*, 220.
[19] D.-Y. Kim, D. Vijayan, R. Praveenkumar, J.-I. Han, K. Lee, J.-Y. Park, W.-S. Chang, J.-S. Lee, Y.-K. Oh, *Bioresour. Technol.* **2016**, *199*, 300.
[20] T. Lafarga, A. Sánchez-Zurano, S. Villaró, A. Morillas-España, G. Acién, *Trends Food Sci. Technol.* **2021**, *116*, 176.
[21] K. Vasilev, S. S. Griesser, H. J. Griesser, *Plasma Processes Polym.* **2011**, *8*, 1010.
[22] B. R. Coad, P. Favia, K. Vasilev, H. J. Griesser, *Plasma Processes Polym.* **2022**, *19*, 2200121.
[23] K. Vasilev, *Coatings* **2019**, *9*, 654.
[24] W. C. Huang, R. Ying, W. Wang, Y. Guo, Y. He, X. Mo, C. Xue, X. Mao, *Adv. Funct. Mater.* **2020**, *30*, 2000644.
[25] B. Saleh, H. K. Dhaliwal, R. Portillo-Lara, E. Shirzaei Sani, R. Abdi, M. M. Amiji, N. Annabi, *Small* **2019**, *15*, 1902232.
[26] B. Ghimire, E. J. Szili, B. L. Patenall, P. Lamichhane, N. Gaur, A. J. Robson, D. Trivedi, N. T. Thet, A. T. A. Jenkins, E. H. Choi, *Plasma Sources Sci. Technol.* **2021**, *30*, 035009.
[27] N. Bezverkhnii, N. Monakhov, M. Petrenko, T. Lapushkina, V. Sakharov, S. Poniaev, S. Bobashev, *J. Phys.: Conf. Ser.* **2020**, *1697*, 012210.
[28] R. Zhou, X. Zhang, Z. Bi, Z. Zong, J. Niu, Y. Song, D. Liu, S. Yang, *Appl. Environ. Microbiol.* **2015**, *81*, 5257.

[29] X. Zhang, R. Zhou, K. Bazaka, Y. Liu, R. Zhou, G. Chen, Z. Chen, Q. Liu, S. Yang, K. Ostrikov, *Plasma Processes Polym.* **2018**, *15*, 1700241.
[30] M. Yusupov, A. Bogaerts, S. Huygh, R. Snoeckx, A. C. T. van Duin, E. C. Neyts, *J. Phys. Chem. C* **2013**, *117*, 5993.
[31] O. Lunov, V. Zablotskii, O. Churpita, A. Jäger, L. Polívka, E. Syková, A. Dejneka, Š. Kubinová, *Biomaterials* **2016**, *82*, 71.
[32] C. Huang, Q. Yu, F. h. Hsieh, Y. Duan, *Plasma Processes Polym.* **2007**, *4*, 77.
[33] C. N. Flynn, C. P. Byrne, B. J. Meenan, *Surf. Coat. Technol.* **2013**, *233*, 108.
[34] K. D. Weltmann, E. Kindel, T. von Woedtke, M. Hähnel, M. Stieber, R. Brandenburg, *Pure Appl. Chem.* **2010**, *82*, 1223.
[35] V. R. Kearns, J. Tasker, Zhuola, R. Akhtar, A. Bachhuka, K. Vasilev, C. M. Sheridan, R. L. Williams, *J. Mater. Sci.: Mater. Med.* **2017**, *28*, 124.
[36] X. Lu, G. V. Naidis, M. Laroussi, S. Reuter, D. B. Graves, K. Ostrikov, *Phys. Rep.* **2016**, *630*, 1.
[37] S. Cheeseman, Z. Shaw, J. Vongsvivut, R. J. Crawford, M. F. Dupont, K. J. Boyce, S. Gangadoo, S. J. Bryant, G. Bryant, D. Cozzolino, *Molecules* **2021**, *26*, 3890.
[38] J. Vongsvivut, D. Pérez-Guaita, B. R. Wood, P. Heraud, K. Khambatta, D. Hartnell, M. J. Hackett, M. J. Tobin, *Analyst* **2019**, *144*, 3226.
[39] A. Shchukarev, Z. Gojkovic, C. Funk, M. Ramstedt, *Appl. Surf. Sci.* **2020**, *526*, 146538.
[40] M. C. Biesinger, *Appl. Surf. Sci.* **2022**, *597*, 153681.
[41] S.-H. Oh, J. Ahn, D.-H. Kang, H.-Y. Lee, *Mar. Biotechnol.* **2011**, *13*, 205.
[42] S. Hao, S. Li, J. Wang, L. Zhao, Y. Yan, T. Wu, J. Zhang, C. Wang, *Mar. Drugs* **2019**, *17*, 362.
[43] A. Dev, S. J. Mohanbhai, A. C. Kushwaha, A. Sood, M. N. Sardoiwala, S. R. Choudhury, S. Karmakar, *Acta Biomater.* **2020**, *109*, 121.
[44] A. Vaishampayan, E. Grohmann, *Microorganisms* **2021**, *10*, 61.
[45] M. A. Kohanski, D. J. Dwyer, B. Hayete, C. A. Lawrence, J. J. Collins, *Cell* **2007**, *130*, 797.
[46] S. Tsuchiya, M. Yamabe, Y. Yamaguchi, Y. Kobayashi, T. Konno, K. Tada, *Int. J. Cancer* **1980**, *26*, 171.
[47] L. J. Leslie, P. Vasanthi Bathrinarayanan, P. Jackson, J. A. Mabiala Ma Muanda, R. Pallett, C. J. Stillman, L. J. Marshall, *Inhalation Toxicol.* **2017**, *29*, 126.
[48] Y. Jeong, W.-Y. Choi, A. Park, Y.-J. Lee, Y. Lee, G.-H. Park, S.-J. Lee, W.-K. Lee, Y.-K. Ryu, D.-H. Kang, *Sci. Rep.* **2021**, *11*, 4906.
[49] T. Korn, E. Bettelli, M. Oukka, V. K. Kuchroo, *Annu. Rev. Immunol.* **2009**, *27*, 485.
[50] N. Ninan, A. Forget, V. P. Shastri, N. H. Voelcker, A. Blencowe, *ACS Appl. Mater. Interfaces* **2016**, *8*, 28511.
[51] Y. Wei, J. Niu, L. Huan, A. Huang, L. He, G. Wang, *Algal Res.* **2015**, *8*, 135.
[52] G. Beamson, D. Briggs, *High Resolution XPS of Organic Polymers*, Wiley, New York **1992**.
[53] M. DuBois, K. A. Gilles, J. K. Hamilton, P. t. Rebers, F. Smith, *Anal. Chem.* **1956**, *28*, 350.
[54] J. Cotas, A. Leandro, P. Monteiro, D. Pacheco, A. Figueirinha, A. M. Gonçalves, G. J. da Silva, L. Pereira, *Mar. Drugs* **2020**, *18*, 384.
[55] A. Bennett, L. Bogorad, *J. Cell Biol.* **1973**, *58*, 419.
[56] K. Thaipong, U. Boonprakob, K. Crosby, L. Cisneros-Zevallos, D. H. Byrne, *J. Food Compost. Anal.* **2006**, *19*, 669.
[57] J. B. Omajali, I. P. Mikheenko, T. W. Overton, M. L. Merroun, L. E. Macaskie, *J. Chem. Technol. Biotechnol.* **2019**, *94*, 295.
[58] Z. Mojtahedi, B. Khademi, S. B. Hashemi, S. M. B. Abtahi, M. A. Ghasemi, M. J. Fattahi, A. Ghaderi, *Oncol. Res.* **2011**, *17*, 7.